

Phase-resolving simulation of dense bubble clusters under periodic shear

Heitkam, S.; Fröhlich, J.;

Originally published:

November 2018

Acta Mechanica 230(2019)2, 645-656

DOI: <https://doi.org/10.1007/s00707-018-2270-8>

Perma-Link to Publication Repository of HZDR:

<https://www.hzdr.de/publications/Publ-28168>

Release of the secondary publication
on the basis of the German Copyright Law § 38 Section 4.

Phase-resolving simulation of dense bubble clusters under periodic shear

Sascha Heitkam · Jochen Fröhlich

Received: date / Accepted: date

Abstract The paper studies the response of a cluster of bubbles to osmotic pressure, and steady and oscillatory shearing by resolved numerical simulations. In contrast to other investigations, the movement of the interstitial fluid is fully resolved. To that end, an immersed-boundary method is employed, yielding the trajectory of each bubble and the flow and pressure field of the fluid. Additionally, a physically motivated collision model ensures realistic bubble interactions. Furthermore, a suitable numerical configuration is proposed which allows imposing osmotic pressure and shear in a way that integrates well into the simulation without generating artefacts. This method allows for the realistic investigation of the compression of bubbles across the jamming limit, demonstrating the influence of the inertia of the interstitial fluid. Applying oscillatory shearing with varying osmotic pressure, shear stress and frequency, the occurrence of shear bands is demonstrated and the influence on rheometric measurements is discussed.

Keywords Bubbles · Simulation · Rheology · Foam

1 Introduction

The flowing behavior of foam is very complex, due to the interaction of several mechanisms such as drainage of liquid, attraction, repulsion, sliding motion

S. Heitkam

Institute of Process Engineering and Environmental Technology, Technische Universität Dresden, 01069 Dresden, Germany

J. Fröhlich

Institute of Fluid Mechanics, Technische Universität Dresden, 01069 Dresden, Germany

Tel.: +49-351-463-37607

Fax: +49-351-463-35246

E-mail: Jochen.Froehlich@tu-dresden.de

or coalescence of bubbles, or distribution of surfactants. Understanding and simulating the flow of foam is interesting on its own, but could also help to improve industrial processes like froth flotation, food technology or production of insulation devices. To that end, a constitutive law is required, linking the stress σ and the corresponding strain rate $\dot{\gamma}$ [1].

Such data is usually obtained in a rheometer. However, measuring foam in a rheometer is not an easy task [2], especially for high shear rates [3]. The stress in general is small, requiring very sensitive torque measurements. Because of the yield stress of foam, special precautions have to be taken to avoid slip between foam and wall. Also, due to drainage the liquid content might change over time. This can be avoided by constantly feeding liquid to the top of the foam in a steady drainage setup. At high liquid fractions, however, convective rolls are induced disturbing the shearing motion [4]. Consequently, rheometer measurements are only applicable for low liquid fraction. For high liquid fractions Φ close to the jamming transition point of $\Phi_c = 0.64$, experiments with concentrated emulsions have yielded interesting insights [5]. However, due to the significantly higher density of the dispersed phase the dynamics might not be completely comparable to foam.

Another way of probing the rheology of wet foam close to the jamming transition is to perform numerical simulations. Durian [6] modeled bubbles as spherical objects interacting via a simplified collision model. This approach has been adapted by several later studies, generally using a spring-dashpot-interaction between the spheres [7–10]. Most of these investigations, however, do not resolve the flow of the interstitial liquid.

The liquid is only taken into account by an adapted collision model describing the interaction of the spherical objects when close to contact. In the case of foam the situation is particular due to the low density of the bubbles compared to the interstitial liquid. This gives rise to the question whether its inertia plays any role with dynamic loading.

In the present study, we will also use such a wet collision model for the contact of spherical bubbles. It has been constructed specifically for bubbles based on detailed physical considerations [11]. Additionally, the interstitial liquid flow together with the corresponding forces on the bubbles is resolved. This extended modeling can also be applied far below the jamming limit.

2 Material and Methods

2.1 Numerical method

The simulations were carried out with the in-house code PRIME [12,13]. It solves the three-dimensional, unsteady Navier-Stokes equation (NSE) for incompressible fluids on a staggered Cartesian grid to describe the liquid motion. Gravity forces are excluded in this study, which is a particular advantage of the simulation approach, because gravity usually yields substantial inhomogeneity of the foam properties experiments. The bubbles are treated as light spheres,

using an immersed-boundary method [14]. Their surface is represented by a number of Lagrangian marker points. At these points, additional volume forces are introduced into the NSE, ensuring a no-slip boundary condition between bubble and liquid. The counteracting forces are included in an equation of motion for each bubble, yielding its velocity and rotation. However, if the surfaces of two bubbles are less than two grid points away from each other, the liquid motion between them is not sufficiently resolved by the fluid grid, yielding an underestimation of the forces in this area. Thus, the Lagrangian points in this region are switched off and additional collision forces are introduced in the bubbles equation of motion. The collision forces are derived from an explicit model only relying on material parameters (given in Table 1), distance deficit $\Delta = R_1 + R_2 - |\mathbf{x}_{c,1} - \mathbf{x}_{c,2}|$ and relative velocity $\mathbf{u}_r = (\mathbf{u}_2 - \mathbf{u}_1)$ with normal and tangential contribution $u_{r,n}$ and $u_{r,t}$, respectively.

It includes an elastic normal force $F_{\text{elastic}}^{\text{coll}}$ accounting for the deformation of the bubble, a dissipative normal force $F_{\text{viscous}}^{\text{coll}}$ accounting for unresolved viscous flow in the collision zone, and a dissipative tangential force $F_{\text{tang}}^{\text{coll}}$ accounting for viscous friction on tangential movement. These forces are defined as

$$\frac{F_{\text{elastic}}^{\text{coll}}}{R_0\sigma} = 18.5 \left(\frac{\Delta}{R_0} \right)^2 + 2.0 \frac{\Delta}{R_0} \quad (1)$$

$$F_{\text{viscous}}^{\text{coll}} = u_{r,n} \mu_f K \left(\frac{\Delta}{R_0} + 0.0002 \right)^{-0.5} f(R_0, \Delta, h_0) \quad (2)$$

$$F_{\text{tang}}^{\text{coll}} = \frac{16}{5} \pi \mu_f u_{r,t} R_0 \ln \left(\frac{h_0}{R_0} \right). \quad (3)$$

Detailed information on the model, the constant K and the function $f(R_0, \Delta, h_0)$ are given in [11]. This model contains the thickness of a stagnant film h_0 as a parameter, resulting from the relative impact velocity between two colliding bubbles. However, if the bubbles form stagnant clusters such an impact velocity loses relevance. The stagnant film thickness is set to $h_0 = 1\mu\text{m}$ which is a compromise between impacting bubbles ($h_0 \approx 5\mu\text{m}$) and steady contact ($h_0 \approx 100\text{nm}$) [15].

2.2 Setup

The numerical setup is depicted in Figure 1. Simulations were carried out in a rectangular domain which is periodic in horizontal directions and bounded by a free-slip wall in vertical direction. The domain contains 200 fully mobile bubbles with a box-shaped distribution of the bubble radius $1.1\text{ mm} \leq R_i \leq 1.3\text{ mm}$, with the index i designating an individual bubble, so that the mean radius is $R_0 = 1.2\text{ mm}$. Additionally, 33 confining bubbles form a soft upper confinement for the fully mobile bubbles. The same is employed at the opposite site. Hence, in total 266 bubbles are simulated. The confining bubbles can move

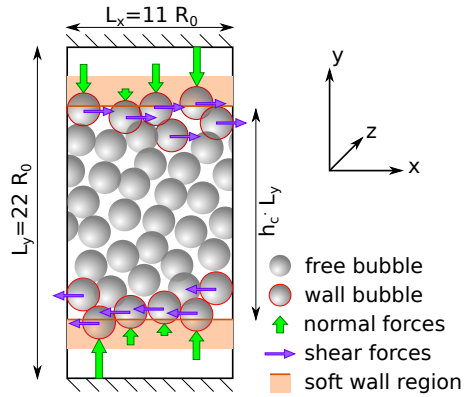


Fig. 1: Setup for the numerical investigation showing the domain, the softwall region (orange areas) confining the mobile bubbles by a factor h_c . Arrows represent the normal (green) and shear (purple) forces applied in the softwall region.

freely as well but in addition experience a vertical force when approaching a certain vertical position, called softwall here and marked in Figure 1. The purpose of this configuration is to mimic an infinitely large bubble cluster. In the horizontal directions this is achieved by periodic boundary conditions. However, if all three directions were periodic, no compression or dynamic shearing could be introduced. Thus, in the vertical direction adjustable walls are applied. If the walls are solid and flat, this induces the formation of layers close to the wall, which in turn biases the shearing behavior. For that reason the softwall approach was designed. The distance between both softwalls $h_c L_y$ is expressed by the relative distance h_c and the domain height L_y . For ease of computation the normal collision forces between bubble and softwall are computed with the same algorithm that provides the collision forces between two bubbles, here adjusted to the present needs:

$$\frac{F_{\text{elastic}}^{\text{wall}}}{R_0 \sigma} = \frac{1}{10} \frac{2(R_i - R_0)}{R_0} \left[18.5 \left(\frac{\Delta_{sw}}{R_0} \right)^2 + 2.0 \frac{\Delta_{sw}}{R_0} \right] \quad (4)$$

$$F_{\text{viscous}}^{\text{wall}} = \frac{1}{10} \frac{2(R_i - R_0)}{R_0} \left[u_{r,n} \mu_f K \left(\frac{\Delta_{sw}}{R_0} + 0.0002 \right)^{-0.5} f(R_0, \Delta_{sw}, h_0) \right] \quad (5)$$

This softwall region is designed to emulate the behaviour of an infinite domain filled with bubbles. Therefore, the collision forces for a given overlap Δ_{sw} between bubble surface and softwall are by a factor of 10 smaller than collision forces that would arise from the overlap with a bubble. Consequently, bubbles do not penetrate the softwall as they would penetrate a rearrangeable bubble cluster. Also, the collision force with the softwall depends linearly on the radius and is 17 % larger than average for the largest bubbles in the present distribution. This follows the idea that smaller bubbles do more easily find a gap in an existing cluster than larger bubbles. In that way, the formation

of crystalline bubble structures at the softwall is effectively suppressed (see Figure 2a).

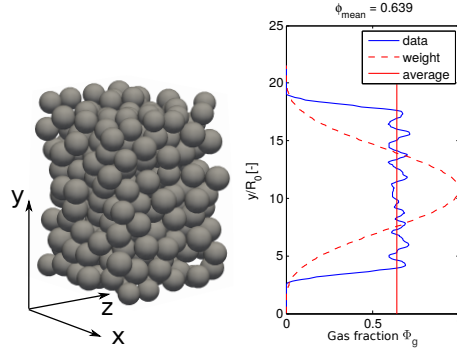


Fig. 2: Bubble cluster under compression. (a) Resulting static bubble positions, (b) corresponding distribution of gas fraction over height for medium confinement of $h_c = 0.80$.

The confining bubbles can also be exposed to an oscillatory tangential force with amplitude τ_0 and frequency ω_0 , inducing shearing motion. The instantaneous shear force is distributed equally to all 33 confining bubbles and introduced in their equation of motion. The fluid is not influenced by the softwall. Important physical and numerical parameter as well as similarity numbers are summarized in Table 1.

In the present investigation a no-slip condition was imposed at the bubble surfaces. This accounts for surfaces fully covered with surfactant rigidifying the surface [16]. In studies of foam rheology the no-slip condition is realistic because usually high amounts of surfactants are employed in such experiments to generate stable bubble sizes as, for example, by Denkov et al. [17,18].

Considerable effort was spent on devising the setup proposed here taking care that the boundaries of the computational domain do not generate artefacts or behavior that differs too much from the one in the core of the domain. If this is not achieved much larger domains might have to be used. Possible artefacts are crystalline bubble layers that would result in an anisotropic effective viscosity. The soft-wall avoids this problem, as depicted in figure 2b. The factor of 10 in the force and the inhomogeneous size-dependency were chosen based on various tests in case of static compression. When using a factor of 1, 2 or 5 artificial layering of bubbles was still observed to some extent, e.g. corresponding to peaks of more than 20 % in Figure 2b. If the factor is 10 or somewhat larger a nearly homogeneous distribution is achieved. Factors substantially larger than 10, however, results in a very small slope of the gas fraction between 0 and 0.6 gas fraction at the border of the cluster in Figure 2b, so that the boundary of the cluster is not well defined. As a result, some bubbles stick out of the cluster and are easily moveable in horizontal

Table 1: Physical and numerical parameter of the simulations conducted.

parameter	symbol	value
bubble diameter	R_i	$1.1 \text{ mm} \leq R_i \leq 1.3 \text{ mm}$
mean bubble diameter	R_0	1.2 mm
gas density	ρ_b	12 kg m^{-3}
surface tension	σ	0.03 Pa m
liquid density	ρ_f	1000 kg m^{-3}
liquid viscosity	μ_f	0.001 Pa s
total number of bubbles	N_b	266
bubbles in one softwall		33
domain size	$L_x \times L_y \times L_z$	$13.3 \times 26.6 \times 13.3 \text{ mm}^3$
lagrangian points per bubble		1692
grid points for fluid	$n_x \times n_y \times n_z$	$128 \times 256 \times 128$
spatial resolution		100 μm
temporal resolution		20 μs
reference pressure	$p_{ref} = \sigma/R_0$	25 Pa

direction because they lose contact to it, which would bias the shear studies relying on a compact cluster.

3 Results

3.1 Static compression

In a first investigation, only normal collision forces and no tangential forces were introduced in the softwall region as described in Section 2.2. Decreasing the distance h_c between the softwalls causes a compression process of the bubble cluster, then reaching a stationary state. The sum of the normal forces introduced in the softwalls by definition yields the osmotic pressure p_{osm} of the bubble cluster [19]. The corresponding gas fraction is derived by computing the gas fraction in horizontal slices and then averaging over height, employing a \sin^2 weight function and proper normalization. Figure 2 shows a snapshot of a stationary bubble cluster, the weight function and the evolution of osmotic pressure and gas fraction over time. The \sin^2 weight is necessary, because the average liquid fraction from a box-shaped weight would be strongly dependent on the position of the edge of the box.

Now, different random initial bubble positions are considered, all with $\Phi_g = 0.5$. In separate simulations different distances h_c between the softwalls were imposed, resulting in different osmotic pressures and different gas fractions. Figure 3 reports on the relation between final, stationary gas fraction and osmotic pressure. In some cases a stationary state was not completely reached. Thus, plotted values result from fitting an exponential function to the development of the gas fraction in time and determining the asymptotic value. The results are sufficiently independent from the initial bubble distribution and

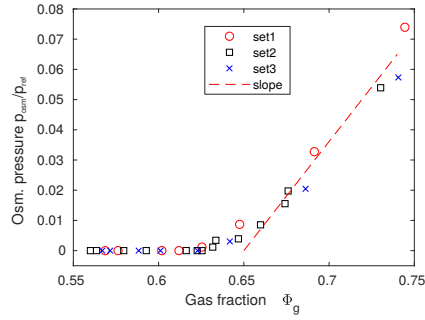


Fig. 3: Gas fraction resulting from different osmotic pressure applied in the softwall region. Each symbol represents the final stationary state of an individual simulation. These were started with three different, randomly generated initial bubble distributions (labeled set 1 - set 3).

show a clear relation. The gas fraction for vanishing osmotic pressure equals approximately 62 %, which is about 3% smaller than the theoretical value of 64 % for random close packing. This might result from the fact, that the periodic boundary conditions impose a periodic structure, deviating from the perfectly relaxed state. The collision model should not be at the origin, because it does not contain any static friction and thus, collision forces vanish in the steady state at the jamming limit. The slope of the curve, indicated by the line in figure 3, is about

$$\frac{\Delta p_{osm}/p_{ref}}{\Delta \Phi_g} = 0.72. \quad (6)$$

This value is in agreement with findings on the static osmotic pressure in monodisperse emulsions, which scatters roughly between 0.4 and 0.8 [20].

Additionally, the simulations allow to analyze the temporal evolution. Figure 4 shows the temporal evolution of the gas fraction. For small confinements, i.e. confinement below the jamming limit, the gas fraction is monotonically increasing in time. However, for strong confinement, an overshoot of the gas fraction and decaying oscillations towards the steady state are visible. Since the inertia of the bubbles is negligible, this can only be caused by the inertia of the interstitial liquid. This idea can be supported by modelling the cluster by a damped spring pendulum. The mass m_s is given by the mass of the interstitial fluid, the damping d_s by the viscous flow through packed spheres (Blake equation []) and the spring stiffness k_s by the stiffness of the cluster under compression, as measured in Figure 3. From this, one can derive an equation of motion for the position x_s of the outer rim of the cluster

$$0 = k_s x_s + d_s \dot{x}_s + m_s \ddot{x}_s \quad (7)$$

$$m_s = \rho_f \Phi_g \approx 400 \quad (8)$$

$$d_s = 72 \frac{\mu_f}{4R_0} \frac{\Phi_g^2}{(1 - \Phi_g)^3} \approx 2 \cdot 10^4 \quad (9)$$

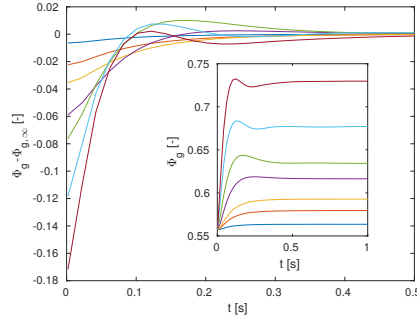


Fig. 4: Evolution of the gas fraction over time for static compression. The same initial bubble distribution is confined with different distances between the softwalls h_c , yielding different evolutions of the gas fraction Φ_g toward the steady state $\Phi_{g,\infty}$.

$$k_s = \frac{\partial p_{osm}}{\partial \Phi_g} \frac{\partial \Phi_g}{\partial x_s} \frac{2}{h_c} \approx 1 \cdot 10^5. \quad (10)$$

from these approximations follows the undamped angular frequency $f_s = \sqrt{k_s/m_s}/2\pi \approx 2.5\text{Hz}$ and the damping ratio $\zeta = 0.5d_s/\sqrt{m_s k_s} \approx 1.5$. This means, the system is slightly overdamped but close to critically damped. Thus, in case of stronger confinement a small overshoot occurs. Also, the corresponding timescale corresponds with the undamped angular frequency.

3.2 Steady shearing

In the next step, a constant tangential shear stress τ_0 is applied in one softwall region and the counteracting stress $-\tau_0$ in the opposite region, as described in Section 2.2. For strong shear stress this results in monotonously increasing global shear deformation α of the cluster. The corresponding global shear rate $\dot{\gamma}(t) = \partial\alpha/\partial t$ is computed from the two times 33 confining bubbles by dividing their average horizontal velocity by the average of their vertical distance, i.e.

$$\dot{\gamma}(t) = \frac{\sum_{i=1}^{33} u_i(t) - \sum_{i=34}^{66} u_i(t)}{\sum_{i=1}^{33} y_i(t) - \sum_{i=34}^{66} y_i(t)}. \quad (11)$$

The corresponding osmotic pressure is derived by summing up the vertical collision forces $f_{i,y}^{coll}$ experienced by bubbles in contact with the softwall, appearing on one side

$$p_{osm}(t) = \frac{\sum_{i=1}^{33} f_{y,i}^{coll}(t) - \sum_{i=34}^{66} f_{y,i}^{coll}(t)}{2L_x L_z}. \quad (12)$$

Figure 5 shows the resulting deformation rate $\dot{\gamma}$, gas fraction and osmotic pressure as a function of the normalized shear stress. The error bars visualize the standard deviation of the respective quantity, which is a measure for the

fluctuations that occur during shearing. Below a certain threshold, the so-called yield stress, the deformation rate equals zero. Above this threshold, the cluster starts to yield.

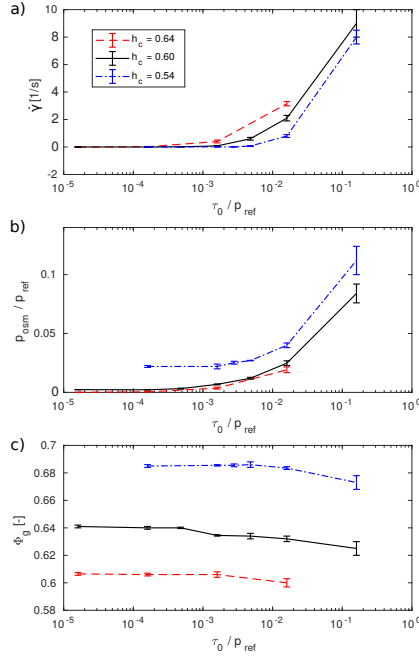


Fig. 5: Steady shear of bubble clusters. (a) Deformation rate, (b) osmotic pressure, and (c) resulting gas fraction as a result of the applied shear stress τ_0 with different levels of confinement h_c . Error bars indicate the fluctuations.

Figure 6 shows the shear stress as a function of the deformation rate. The yield stress was derived by fitting a Herschel-Bulkley law [21]. In case of the weakest confinement no yield stress is present, which is in agreement with [22]. The insert in Figure 6 links the derived yield stress to the corresponding osmotic pressure derived from Figure 5b. In good approximation the yield stress depends linearly on the osmotic pressure. The yield stress increases with increasing gas fraction. Along with the yielding, the osmotic pressure for a given confinement increases and the gas fraction decreases. This is due to the effect of dilatancy [23]. Beyond the values provided, the good agreement with the Herschel-Bulkley law demonstrates that the somewhat involved construction of the boundary conditions pays off, in that it provides the same behaviour as in a large volume.

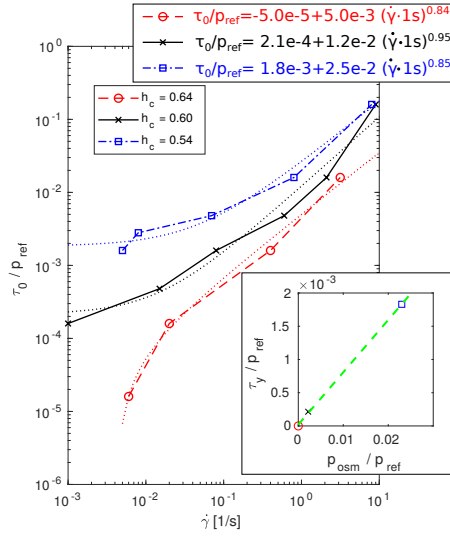


Fig. 6: Estimation of yield stress by least-square fitting of the stress-strain relation with the Herschel-Bulkley relation. Inset: relation between yield stress and osmotic pressure at the yield point.

3.3 Dynamic shearing

Now, after the stationary state of static compression is reached, oscillating tangential stress $\tau = \tau_0 \cos(\omega_0 t)$ is applied, resulting in an oscillatory shearing motion of the cluster. Figure 7 shows the average amplitude and the phasing of the shear rate as a function of the confinement h_c , the applied tangential stress amplitude τ_0 and its frequency ω_0 . Figure 7a and 7b demonstrate the influence of the shear stress on the shear rate for a constant frequency of $2Hz$. For purely solid behavior, the phase shift between force and shear rate should be -90 degrees, for purely viscous behavior it should be 0 degrees, and for purely inertial behavior it should equal $+90$ degrees. In each of these cases, the amplitude of the shear rate would be proportional to the amplitude of the applied stress. Indeed, Figure 7a shows a linear relation between shear force and shear rate amplitude. Surprisingly, the relation seems to be fairly independent of the confinement. Figure 7b provides the phase shift. For medium confinement, the phase shift is about 40 degrees, marking viscous-inertial behavior. For stronger confinement, the behavior tends toward a solid-like characteristic, even reaching negative phase shifts. For very weak confinement the phase shift is high, pointing towards inertia-dominated behavior. Figure 7c and 7d demonstrate the influence of the frequency on the shear rate for a medium shear stress of $\tau_0/(\sigma/R) = 0.0016$. With increasing frequency, the shear rate decreases, because less momentum is transferred into the foam. The phase shift grows with frequency, because elastic forces are independent of the frequency, viscous forces depend linearly and inertial forces depend quadratically

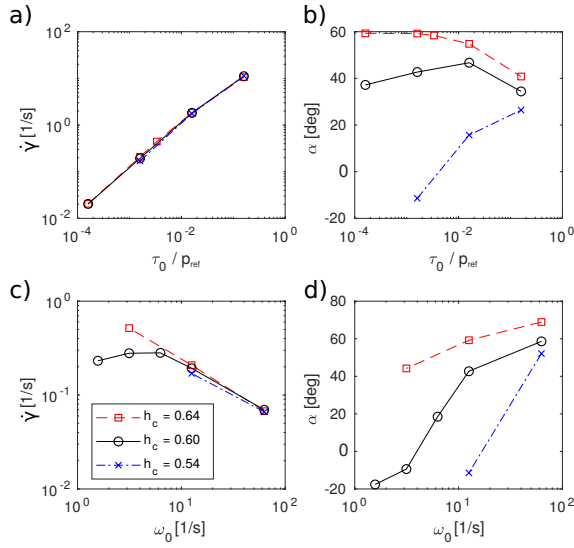


Fig. 7: Deformation rate $\dot{\gamma}$ and corresponding phase shift α for clusters exposed to oscillatory shear stress. (a) and (b) dependency on amplitude of shear stress for three different levels of confinement with a fixed frequency of $\omega_0/2\pi = 2Hz$. (c) and (d) dependency on frequency of shear stress for three different levels of confinement with a fixed shear stress amplitude $\tau_0/(\sigma/R_{mean}) = 0.0016$.

on the frequency. Consequently, inertial forces have a larger influence at higher frequencies.

In order to investigate the distribution of the deformation rate throughout the cluster, the velocity of the bubbles was computed in 256 horizontal slices, averaging the velocities of the adjacent bubbles using the volume fraction of the bubbles inside the slice as a weight. Note, that this shear rate is based on the bubbles alone, not the interstitial fluid, so that it is zero outside the cluster. Figure 8 shows the shear rate over height at different instances in time for seven selected cases. It is interesting to note, that in the topmost row the macroscopic shear is independent of the confinement, which is also plotted in Figure 7a. However, Figure 8 shows that the corresponding distribution of shear inside the cluster and, therefore, the rheological behavior is completely different. For strong confinement shearing is linearly distributed, as would be the case for purely elastic or viscous behavior.

At medium confinement a wave is visible corresponding to the interaction of elastic and inertial behavior. The elastic behavior results from the elastic contribution in the collision model while the inertial behavior is caused by the inertia of the interstitial fluid.

For weak confinement, and also for high frequencies and high shear stresses, a jump in the horizontal velocity is visible at $y/R_0 \approx 5$ and 17, corresponding to the formation of a shear band between the softwall and the free bubble

cluster. Similar shear bands have been detected in several other simulations (not presented here) showing the same tendency.

3.4 Complex shear modulus

The most convincing way to derive a constitutive law from the dynamic shearing would possibly be to fit the shear rate over height and time with a wave equation, as done by Costa et al. [3] for rheometric measurements of relatively dry foam. However, in wet foam (under weak confinement) shear bands can occur which is not described by the wave equation. To demonstrate the difficulties, three cases with moderate amplitude and frequency are discussed here, the ones presented in the topmost row of Figure 8. The time-dependent horizontal velocity $\bar{u}(y, t)$ for each horizontal layer is derived by averaging the horizontal velocity $u_i(t)$ of the intersected bubbles using the intersectional area $A_i(y)$ as a weight

$$\bar{u}(y, t) = \frac{\sum_{i=1}^{266} u_i(t) A_i(y)}{\sum_{i=1}^{266} A_i(y)}. \quad (13)$$

The time-dependent elongation $\bar{x}(y, t)$ is derived by integrating the averaged horizontal velocity $\bar{u}(y, t)$ in time with a central differences scheme. Based on this quantity, the complex amplitude of elongation $X_0^*(y)$ is derived by integrating over one period

$$X_0^*(y) = \frac{1}{T} \int_0^T e^{i\omega_0 t} \bar{x}(y, t) dt \quad (14)$$

The complex solution $\tilde{X}_0^*(y)$ of the wave equation

$$\rho_f(1 - \Phi_g) \frac{\partial^2 \tilde{X}_0^*(y) e^{i\omega_0 t}}{\partial t^2} = G^* \frac{\partial^2 \tilde{X}_0^*(y) e^{i\omega_0 t}}{\partial y^2} \quad (15)$$

should describe the measured values of $X_0^*(y)$. All factors in (15), except G^* , can be determined from the measurements. The gas fraction Φ_g is assumed to be constant over y and to equal the measured average gas fraction. Now, G^* is optimized such that the solution of (15), $\tilde{X}_0^*(y)$, fits the measured data $X_0^*(y)$ at best. This is done by minimizing the sum of the squares of the differences between $\tilde{X}_0^*(y)$ and $X_0^*(y)$. All horizontal layers y that contain less than 50% of this gas fraction are not taken into account for the fit. In that way, the liquid-filled regions above and below the cluster are neglected. Figure 9 shows the real and imaginary part of $\tilde{X}_0^*(y)$ and $X_0^*(y)$ and the values of G^* resulting from the optimization. In the interior of the cluster, the wave equation represents the shearing quite well, however, close to the softwall region the elongation differs from the wave equation, especially in the case of stronger confinement where also the shear band occurs. The reason is that equation 15 assumes constant properties, i.e. constant density and constant G^* throughout the cluster. However, in a shear band higher liquid fraction is

accumulated, resulting in a localized variation of G^* and Φ_g . Consequently, a wave equation with constant values of G^* and density can not capture the behavior.

4 Conclusions

In this study a suitable numerical setup, termed softwall, was developed to introduce osmotic pressure and shear in a periodic representative volume filled with gas bubbles. It minimizes artefacts and turned out to be very well suited for the studies undertaken. Similar studies, on colloids for example, might employ this as well with benefit.

In the coupling between bubbles and fluid the bubbles are assumed spherical. On the other hand, bubble deformation is accounted for by the nonlinear elastic collision force between the bubbles. The spherical shape of the bubbles, imposed by the position of the Lagrangian marker points, enters the computation of the interstitial flow field. This approach is justified for moderate osmotic pressures and gas fractions as investigated here. It loses validity for substantially higher gas fractions because it does not account for the reduced cross-sectional area of plateau borders in compressed foam and, thus, overestimates the liquid flow.

While the numerical method is well suited for simulating large amounts of spheres [24], the employed number of bubbles in this study is limited by the high resolution, the required times for reaching steady states and the number of parameters varied. In fact, a single data point in figure 5, for example, required several weeks on 128 CPUs of a high-performance computer.

The periodic boundary conditions in the horizontal directions and the softwall are employed to represent an infinite bubble cluster. With this approach non-periodic structures larger than the domain size cannot be represented. The videos taken suggest that in the bulk of the cluster the motion is fairly irregular. Furthermore, these very large structures are deemed not decisive for the physics investigated here, the inertial effect of the interstitial fluid. An exception are the shear bands, represented as infinitely large with the present domain if their size is larger than 6 bubbles in one direction. In experiments these shear bands can become extremely long, of the order of several hundred bubble diameters [25], so that the present setup with infinite length is a very good approximation.

The present investigations were concerned with stationary compression, steady shear and oscillatory shear. Figure 4 showed an overshoot of the gas fraction when compressing a bubble cluster. This presumably cannot be reproduced with a numerical method neglecting the flow of the interstitial fluid. At the same time, this is a feature, where colloids substantially differ from foam, because the additional inertia of the droplets would increase the overshoot. Also the inertial-influenced behavior in the dynamic shearing experiment is a feature that cannot be reproduced exactly in simulations that do not take into account the interstitial fluid flow. When modelling, one could artificially

add the mass of the unresolved interstitial fluid to the mass of the spherical objects, but that would neglect the acceleration of the fluid relative to the spherical objects.

Shear bands occurred in our simulations in case of low confinement, high frequencies, or high shear stress (see figure 8). The case of high shear stress is well documented in the literature [25, 1]. The case of high frequency could correlate to the observation of shear bands during start-up of steady shear [26], because high frequency means a continuous accelerating and decelerating, such that the cluster cannot overcome its static yield stress. The case of low confinement has been observed in the opposite way for two-dimensional foam in a Couette-type flow [27]. With continuous shear in dry foam shear banding was found to occur more frequently than in wet foam. The discrepancy might result from the higher frequency in our case. Due to the high liquid fraction sliding layers might form and so that the inner cluster loses contact to the softwall. If, however, steady shear was applied the viscous friction would homogenize the shear rate after some time. Hence, due to the high frequency only the start-up is observed here. Fitting the complex shear modulus to the distribution of the complex shear elongation has demonstrated a significant deviation of the observed behaviour from the wave equation in cases of high frequencies or shear stress. This is due to the formation of shear bands that cannot be described by the wave equation. Consequently, one has to be very careful when applying the wave equation to the values for wet foam or granular material measured in a rheometer.

References

1. S. Cohen-Addad, R. Höhler, O. Pitois, *Annual Review of Fluid Mechanics* **45**(1), 241 (2013)
2. R. Höhler, S. Cohen-Addad, *Journal of Physics: Condensed Matter* **17**(41), R1041 (2005)
3. S. Costa, R. Höhler, S. Cohen-Addad, *Soft Matter* **9**(4), 1100 (2013)
4. S. Hutzler, D. Weaire, R. Crawford, *EPL (Europhysics Letters)* **41**(4), 461 (1998)
5. S. Cohen-Addad, R. Höhler, *Current Opinion in Colloid & Interface Science* **19**(6), 536 (2014)
6. D. Durian, *Physical Review Letters* **75**(26), 4780 (1995)
7. A. Ngan, *Physica A: Statistical Mechanics and its Applications* **339**(34), 207 (2004). DOI <http://dx.doi.org/10.1016/j.physa.2004.03.068>. URL <http://www.sciencedirect.com/science/article/pii/S0378437104003395>
8. T. Hatano, *Journal of the Physical Society of Japan* **77**(12), 123002 (2008)
9. P. Mills, P. Rognon, F. Chevoir, *EPL (Europhysics Letters)* **81**(6), 64005 (2008)
10. M. Van Hecke, *Journal of Physics: Condensed Matter* **22**(3), 033101 (2009)
11. S. Heitkam, A. Sommer, W. Drenckhan, J. Fröhlich, *Journal of Physics: Condensed Matter* **29**(12), 124005 (2017). DOI 10.1088/1361-648x/aa56fc
12. T. Kempe, J. Fröhlich, *Journal of Computational Physics* **231**(9), 3663 (2012)
13. T. Kempe, *A numerical method for interface-resolving simulations of particle-laden flows with collisions* (TUDpress Verlag der Wissenschaften GmbH, 2013)
14. S. Schwarz, T. Kempe, J. Fröhlich, *Journal of Computational Physics* **281**, 591 (2015)
15. D.Y. Chan, E. Klaseboer, R. Manica, *Soft Matter* **7**(6), 2235 (2011)
16. R. Clift, J.R. Grace, M.E. Weber, *Bubbles, Drops and Particles* (pub, 1978)
17. N. Denkov, S. Tcholakova, K. Golemanov, K. Ananthapadmanabhan, A. Lips, *Physical review letters* **100**(13), 138301 (2008)

18. N.D. Denkov, S. Tcholakova, K. Golemanov, K. Ananthpadmanabhan, A. Lips, *Soft Matter* **5**(18), 3389 (2009)
19. H. Princen, *Langmuir* **2**(4), 519 (1986)
20. R. Hoehler, Y.Y.C. Sang, E. Lorenceau, S. Cohen-Addad, *Langmuir* **24**(2), 418 (2008)
21. I. Cantat, S. Cohen-Addad, F. Elias, F. Graner, R. Höhler, O. Pitois, *Foams: structure and dynamics* (Oxford University Press, 2013)
22. B. Herzhaft, S. Kakadjian, M. Moan, *Colloids and Surfaces A: Physicochemical and Engineering Aspects* **263**(1), 153 (2005)
23. D. Weaire, S. Hutzler, *Philosophical Magazine* **83**(23), 2747 (2003)
24. B. Vowinkel, T. Kempe, J. Fröhlich, *Advances in Water Resources* **72**, 32 (2014)
25. P. Schall, M. van Hecke, *Annual Review of Fluid Mechanics* **42** (2010)
26. F. Rouyer, S. Cohen-Addad, M. Vignes-Adler, R. Höhler, *Physical Review E* **67**(2), 021405 (2003)
27. G. Debregeas, H. Tabuteau, J.M. Di Meglio, *Physical Review Letters* **87**(17), 178305 (2001)

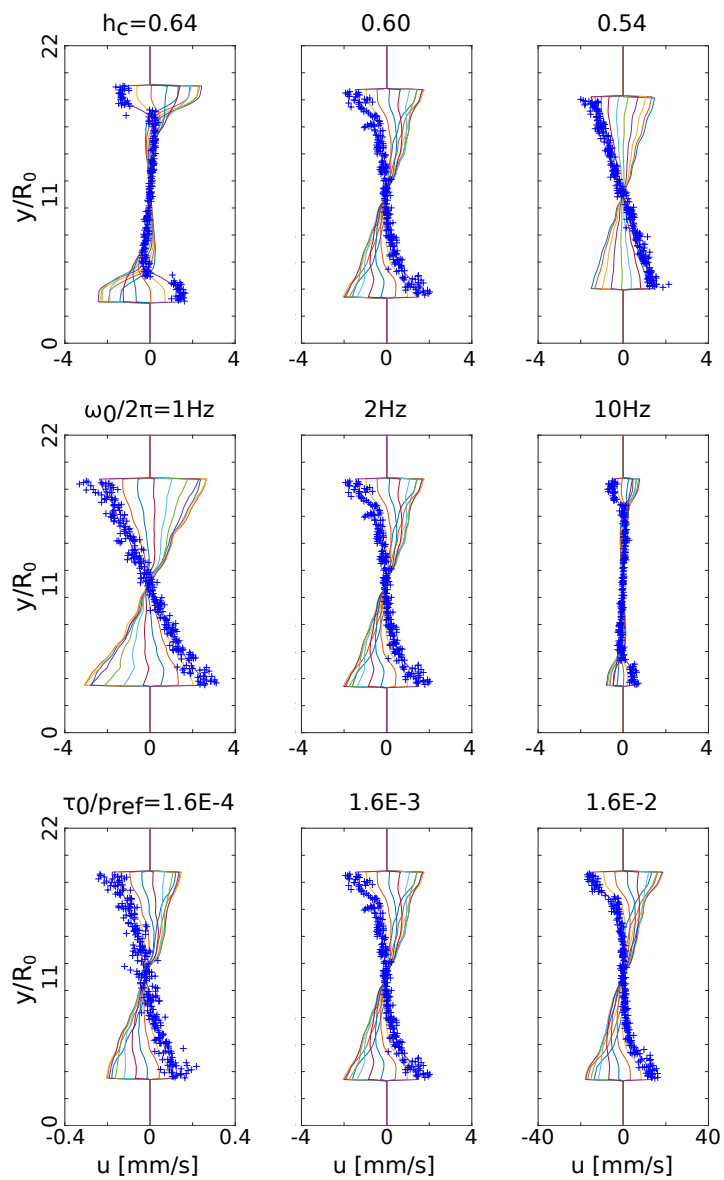


Fig. 8: Horizontally averaged horizontal bubble velocity component over height at ten time instances equally distributed over half a period. Blue crosses mark the velocity versus height of each bubble center at the last time instance. The center column shows three times the identical reference case, each row shows the variation of one parameter. Top: variation of h_c , middle: variation of ω_0 , bottom: variation of τ_0 .

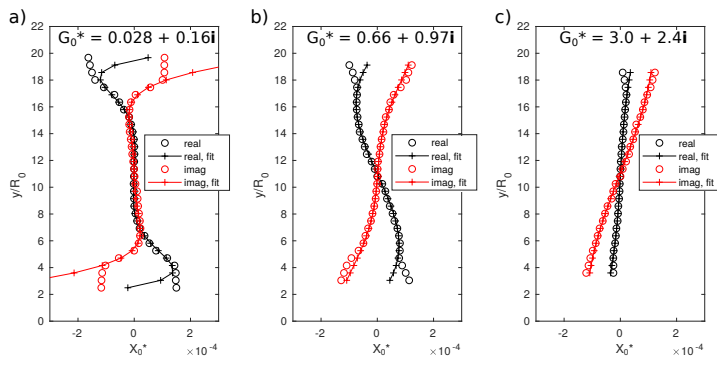


Fig. 9: Real and imaginary part of the complex elongation across the cluster X_0^* and the corresponding result of equation (15) after fitting G_0^* for $\omega_0/2\pi = 2Hz$ and $\tau_0/(\sigma/R_{mean}) = 0.0016$. (a) $h_c=0.64$, (b) $h_c=0.60$, (c) $h_c=0.54$.